PNAS RESEARCH ARTICLE | BIOCHEMISTRY

POTRA domains of the TamA insertase interact with the outer membrane and modulate membrane properties

Abdelkader Mellouk[a,b], Paul Jaouen[b,c], Louis-Jacques Ruel[b,d,e], Michel Lê[a,b], Cyrielle Martini[a,b], Trevor F. Moraes[f], Majida El Bakkouri[g], Patrick Lagüe[b,d,e], Elodie Boisselier[b,c], and Charles Calmettes[a,b,1]

Affiliations are included on p. 11.

Edited by Scott Hultgren, Washington University School of Medicine in St. Louis, St. Louis, MO; received February 8, 2024; accepted May 22, 2024

The outer membrane (OM) of gram-negative bacteria serves as a vital organelle that is densely populated with OM proteins (OMPs) and plays pivotal roles in cellular functions and virulence. The assembly and insertion of these OMPs into the OM represent a fundamental process requiring specialized molecular chaperones. One example is the translocation and assembly module (TAM), which functions as a transenvelope chaperone promoting the folding of specific autotransporters, adhesins, and secretion systems. The catalytic unit of TAM, TamA, comprises a catalytic β-barrel domain anchored within the OM and three periplasmic polypeptide-transport-associated (POTRA) domains that recruit the TamB subunit. The latter acts as a periplasmic ladder that facilitates the transport of unfolded OMPs across the periplasm. In addition to their role in recruiting the auxiliary protein TamB, our data demonstrate that the POTRA domains mediate interactions with the inner surface of the OM, ultimately modulating the membrane properties. Through the integration of X-ray crystallography, molecular dynamic simulations, and biomolecular interaction methodologies, we located the membrane-binding site on the first and second POTRA domains. Our data highlight a binding preference for phosphatidylglycerol, a minor lipid constituent present in the OM, which has been previously reported to facilitate OMP assembly. In the context of the densely OMP-populated membrane, this association may serve as a mechanism to secure lipid accessibility for nascent OMPs through steric interactions with existing OMPs, in addition to creating favorable conditions for OMP biogenesis.

structural biology | biophysics | protein | lipid interactions | membrane biogenesis

Significance

TamA is the catalytic core of the translocation and assembly module, a transenvelope complex facilitating the assembly of specific outer-membrane proteins (OMPs) in gram-negative bacteria. Concealing its catalytic site within the membrane domain, TamA extends three polypeptide-transport-associated (POTRA) domains into the periplasm. Initially considered structural elements responsible for recruiting the auxiliary protein TamB, the POTRA domains were revealed to actively participate in OMP assembly by modulating membrane properties. Exploring the conformational landscape of the POTRAs, we uncovered a membrane-binding site mediating the enrichment of phosphatidylglycerol near the active site, providing a conducive environment for OMP assembly. This finding reveals a unique function of the POTRA domain, enriching our molecular understanding of the critical assembly of virulence factors processed by TamA.

A promising target for combating gram-negative bacteria is the critical bacterial envelope, which includes conserved molecular machines such as the β-barrel assembly machinery (BAM) and translocation and assembly module (TAM) involved in its biogenesis (1–3). The outer membrane (OM) primarily comprises outer membrane proteins (OMPs), which are embedded within the membrane via a β-barrel domain (4). These proteins participate in a variety of essential functions, such as cell division, nutrient uptake, mobility, and signaling, and govern host–pathogen interactions, significantly contributing to adhesion, immune evasion, and toxin delivery (5). Notably, the OMPs are assembled by the BAM, which is composed of the essential and ubiquitous BamA catalytic subunit accompanied by an assortment of different auxiliary lipoproteins whose composition varies from one bacterial species to another. The best-characterized system is the BamABCDE complex in *Escherichia coli* (6).

Although all OMPs require BAM for their assembly, a distinct subset of OMPs, such as the autotransporter Ag43, adhesins FdeC and intimin, the efflux pump TolC, and the usher protein FimD, relies on an additional chaperone machinery known as the translocation and assembly module (TAM) (7–11). The TAM consists of two interacting proteins, TamA and TamB, which associate with one another to form a transenvelope machinery, facilitating the assembly of specific OMP clients (12). TamA resembles BamA and is the outer membrane subunit, while TamB is a large inner membrane protein assisting in the transit of unfolded OMP substrates across the periplasm. The deletion of *tamA* or *tamB* is associated with reduced virulence or colonization potential in various bacterial pathogens, a phenotype attributed to the improper assembly of outer membrane virulence factors (3, 7, 13). TAM was discovered more recently than the ubiquitous BAM system and has received less attention. Therefore, our understanding of TAM has been limited, and the functional model of TamA has been based mainly on knowledge gained from its BamA counterpart. These proteins belong to the OMP85 family and possess a unique β-barrel that opens into the membrane along its seam (β1 to β16) (14–17). This lateral

The authors declare no competing interest.

This article is a PNAS Direct Submission.

[1]To whom correspondence may be addressed. Email: charles.calmettes@inrs.ca.

This article contains supporting information online at https://www.pnas.org/lookup/suppl/doi:10.1073/pnas.2402543121/-/DCSupplemental.

Published July 3, 2024.

gate is dynamic and has been shown to interact with OMP substrates. Notably, the gate influences the insertion of proteins into the OM by disordering nearby lipids, while providing incoming OMP clients with access to the hydrophobic core of the OM (18). This intricate process is supported by auxiliary Bam proteins and further assisted by the exceptionally thin hydrophobic belt surrounding the lateral gate, which exerts localized bending stresses on the membrane. The folding mechanism derived from studies regarding BAM involves the formation of a transient hybrid BamA-OMP barrel at the lateral gate, which eventually dissociates to release the newly assembled β-barrel in the OM (19–22).

Another key architecture of OMP85 proteins resides in the amino-terminal domain, which comprises periplasmic repeats of polypeptide-transport-associated (POTRA) domains. The number of POTRA domains varies within the OMP85 family, with BamA and TamA possessing five and three POTRA domains, respectively (23, 24). The structures of the BamABCDE complex offer valuable insights into the function of POTRA domains as anchor points, enabling the recruitment of auxiliary Bam proteins that facilitate conformational changes within BamA's lateral gate (25, 26). In the case of TamA, POTRA-1 is required for the formation of TAMs by sequestering the carboxy-terminal tail of TamB (12). Furthermore, the complete removal of all POTRA domains has been shown to abolish the chaperone function of TamA in *E. coli* (17).

Although TAM shares multiple similarities with BAM, it also introduces unique characteristics exemplified by a transenvelope architecture (vs. the OM-centric BAM complex), a reliance on BAM-unrelated auxiliary protein, and a disparate POTRA domain layout (horizontally toward the membrane) that imply evolutionary differentiation in the mechanism, specificity, and regulation of TAM (*SI Appendix*, Fig. S1). The role of these unique distinctive elements in TAM, particularly their potential contribution to the insertase function of TamA, remains an open question in the field. The present study focused on elucidating the function of the unique croissant-shaped organization of the POTRA domains in TamA (Fig. 1), which is characterized by a distinctly prolonged architecture parallel to the membrane—a domain arrangement that appears flexible based on different crystal structures of TamA obtained from the opportunistic pathogen *Pseudomonas aeruginosa*. Indeed, the conformational landscape of *Pa*TamA, solved in three different space groups, unveils the dynamic nature of its POTRA domains and suggests a mechanism by which the POTRA arm associates with the OM to modulate its properties. In support of this hypothesis, certain bacterial phyla, such as *Bacteroidetes* and *Chlorobiota*, encode a lipidated TamA variant called TamL, which incorporates a lipid anchor at the amino-terminal region of the POTRA-1 domain (23). To further explore the POTRA–membrane interactions, we applied in silico molecular dynamics (MD) simulations and orthogonal biophysical approaches. Our data provide compelling evidence that the periplasmic domain of TamA can directly associate with the inner leaflet of the OM through a series of polar amino acids (Arg/Lys) lining the POTRA-1/2 domains. When interacting with the membrane, POTRA domains preferentially bind to unsaturated phosphatidylglycerol (PG), leading to a discernable impact on the phase transition temperature. This interaction likely plays a role in recruiting and sustaining a favorable lipid environment, thereby facilitating the insertion of OMP substrates into a fluidic state membrane enriched in PG lipids. This process simultaneously creates room for the incoming nascent OMP to fold into the membrane, which is densely packed with preexisting OMPs (5, 27). Taken together, these findings offer unique insights into the molecular mechanism underlying the function of TamA and contribute to a deeper understanding of how the POTRA domains participate in OM biogenesis and influence the membrane environment.

Results

The TamA Structure Suggests POTRA–Membrane Interactions. The structure of TamA from the model organism *E. coli* was previously solved in bicelles (15). To further explore the structural and conformational landscape of TamA, we attempted to elucidate additional structures using other bacterial models. Successful crystallization in C_8E_4 detergent was achieved with the *P. aeruginosa* TamA homolog (*Pa*TamA), sharing 34% sequence identity with *Ec*TamA. The expression and purification of *Pa*TamA

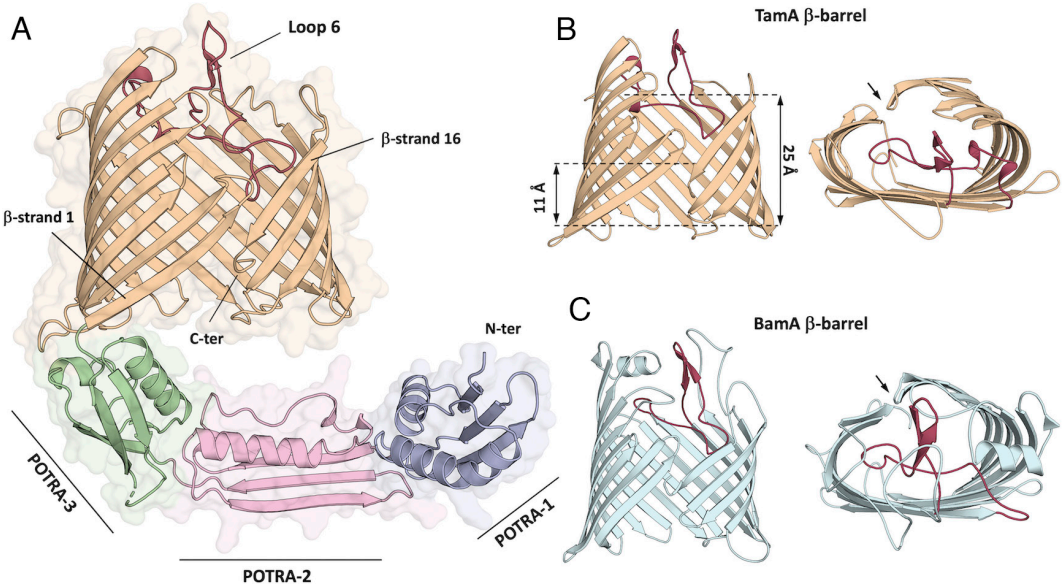

Fig. 1. TamA has a conserved fold with the OMP-insertase BamA. (*A*) Structure of full-length *Pa*TamA in cartoon representation. The outer membrane domain is visualized in beige, and the three periplasmic POTRA domains 1, 2, and 3 are colored blue, pink, and green, respectively. The C-terminal extremity of TamA is characterized by an unzipped β-strand that folds inward within the barrel structure. The lateral gate is constituted by the two β-strands 1 and 16, establishing a passage between the lipidic phase and the barrel lumen. (*B*) and (*C*) represent side and *Top* views of the membrane domains and lateral gates of *Pa*TamA and *Ec*BamA in similar orientations. The black arrows indicate the unzipped junction forming the lateral gate between strands 1 and 16.

were accomplished with high purity and homogeneity, yielding 10 mg of protein per liter of culture. Several crystal forms of full-length *Pa*TamA were collected from space groups C222, $P22_12_1$, and $P2_1$, with the best crystals diffracting to 2.6 Å resolution using selenomethionine derivatized *Pa*TamA proteins. The *Pa*TamA structures maintain the overall architecture observed in *Ec*TamA, harboring a carboxy-terminal β-barrel domain occluded by an extracellular loop to enclose a hydrophilic cavity partially opened on the inner leaflet of the OM (Fig. 1*A*). Like BamA, TamA exhibits an atypical cracked-barrel architecture, lacking hydrogen bonds between strands 1 and 16, which loosely associate to create access from the barrel lumen to the hydrophobic lipid phase. The open seam in *Pa*TamA corresponds to a narrow 11 Å hydrophobic region and is likely involved in membrane perturbation at the substrate insertion site (Fig. 1 *B* and *C*). These singular traits shared by BamA and TamA are proposed to locally disorder the membrane at the seam of the chaperone barrel, where the lateral gate provides a seeding template for the assembly of incoming OMP substrates by sequential β-augmentation events.

The three POTRA domains are exposed to the periplasm and anchored to the membrane by the carboxy-terminal barrel domain. This POTRA arm adopts a croissant-shaped arrangement, extending 80 Å parallel to the membrane, with the amino terminus oriented toward the OM. The multiple *Pa*TamA crystal structures display the dynamic nature of the POTRA domains, allowing significant movements that enable these domains to rearrange toward or away from the OM (Fig. 2*A*). Our various structures illustrate a variety of *Pa*TamA conformations, positioning the POTRA-1 domain at distances ranging from 17 Å to 2 Å in relation to the hydrophilic headgroups of the OM. POTRA-1 appears to be the most mobile element, as indicated by its higher B-factor values, and lack of electron density in the C2 space group. Additionally, the orientations of the three POTRA domains are flexible, permitting conformational adaptability between adjacent POTRA domains (Fig. 2*C*). These multiple conformations represent a possible reorganization adopted by the TAM during OMP assembly. This hypothesis is consistent with the published *Ec*TamA structure which locates the POTRA-1 domain 20 Å away from the membrane (15) and with the findings of an earlier biophysical study using magnetic contrast neutron reflectometry that identified two TamA conformers exhibiting significant vertical amplitude movement (up to 70 Å) upon substrate binding to the POTRA-1/2 domains (9, 12, 28). This structural flexibility indicates that the POTRA domains of TamA could reach the inner surface of the OM and maintain interactions with the polar head groups of phospholipids. This hypothesis is further supported by the evolutionary occurrence of a TamL homolog in the *Bacteroidetes* and *Chlorobiota* phyla (still part of an operon with *tamB*), which encodes a version of TamA that is lipidated at its POTRA-1 amino-terminal residue and is likely to sequester the POTRA domains on the OM (23).

To explore the concept of specialized functions associated with the POTRA domains of TamA and TamL, we performed a comparative analysis of these domains within the BAM and TAM systems. Utilizing cluster analysis of sequences (CLANS) (29), our objective was to uncover potential differences or similarities among these systems. To this end, we aimed to broaden the scope of the previous analysis conducted by Selkrig et al. (12) by incorporating a more extensive representation of sequences encompassing most bacterial lineages that encode the *tamA* or *tamL* gene. While the POTRA-3 domain of the TAM system exhibits notable similarities to that of

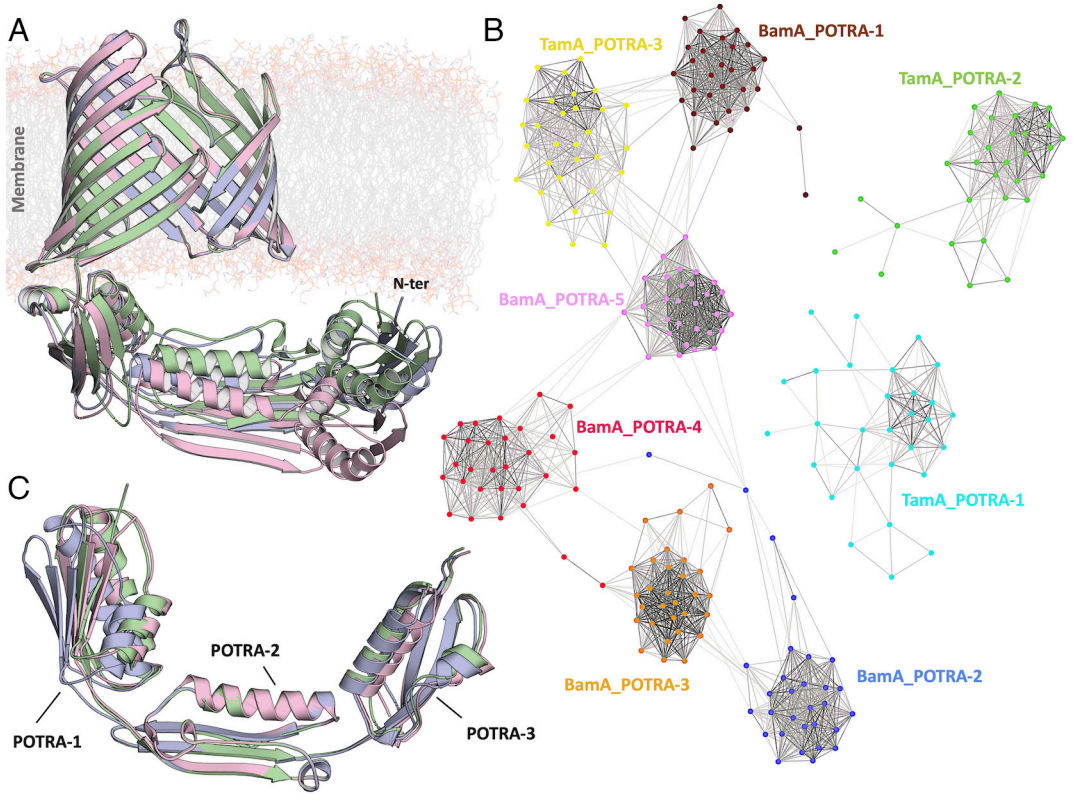

Fig. 2. POTRA domains of TamA are flexible and differ from BamA sequences. (*A*) Structural overlay of the three *Pa*TamA structures solved in this study from three different space groups. The structures are aligned on their membrane domains to illustrate the flexibility of the periplasmic POTRA domains relative to the membrane-embedded β-domain. (*B*) The CLANS analysis depicts an all-against-all pairwise BLAST clustering of individual POTRA sequences of BamA and TamA/TamL from 30 representatives of alpha-, beta-, gamma-, delta-Proteobacteria and Bacteroidetes that encode the BAM and TAM machineries (protein sequences listed in *SI Appendix*, Table S3). Line connections are drawn between similar sequences based on a *P* value cutoff of $1e^{-5}$. (*C*) The POTRA domains solved from the $P2_1$, C2, and $P22_12_1$ space groups (colored as in panel *A*) are aligned on their corresponding POTRA-2 domains to illustrate the intrinsic flexible orientation within the POTRA arms.

the BAM system, a divergence emerges between the POTRA-1 and POTRA-2 domains of the TamA/TamL proteins and corresponding BamA domains (Fig. 2*B*). This divergence alludes to a potential functional differentiation between the two systems that could drive the assembly of a transenvelope complex with TamB (12) and/or promote proximal interaction with the OM.

The POTRA-1 and POTRA-2 Domains Partition onto the Membrane as Indicated by MD Simulations. To investigate the potential interactions between POTRA domains and the bacterial membrane, we conducted three independent 1-μs MD simulation trajectories of the TamA protein in a POPE:POPG (80:20) bilayer, which was designed to mimic the lipid composition of the inner leaflet. Although the TamA transmembrane barrel was in the bilayer, the initial position of the POTRA-1/2 arm was set at least 20 Å from the bilayer surface. However, during the MD trajectories, we observed rapid repositioning of the POTRA-1 and POTRA-2 domains, bringing them closer to the bilayer interface (Fig. 3*A* and *SI Appendix*, Fig. S2). This association with the membrane interface did not cause any major reorganization of the secondary structure in the POTRA domains, as indicated by the RMSD values, which remained below 2.5 Å throughout the simulations (*SI Appendix*, Fig. S3*A*). Moreover, the secondary structure of the POTRA domains remained conserved in the presence of the lipid bilayer, as confirmed by the superposition of the final conformation of the domains onto their respective experimental structures (*SI Appendix*, Fig. S3*B*).

The dynamics of the interactions between the POTRA residues and the lipid components are reported in Fig. 3*B*. Specifically, we

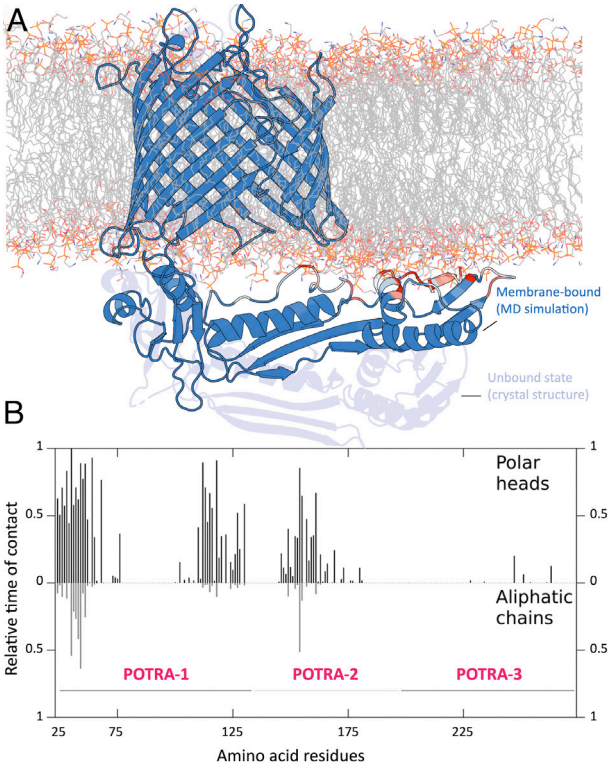

Fig. 3. POTRA domains of TamA associate with POPE:POPG membranes in MD simulations. (*A*) TamA is represented as a cartoon, and the lipids are drawn as sticks (gray for the aliphatic chains and colors for the polar heads). The amino acids from the POTRA domains are colored according to their relative contact time with the lipid polar heads, from blue (no contact) to red (higher times of contact). (*B*) Relative contact times between POTRA-1/2/3 residues and lipid polar heads (*Top*) and aliphatic chains (*Bottom*). Lipids located within 4 Å of the protein residues were used for the calculations. The POTRA segments are identified along the residue sequence.

analyzed the contact times between the POTRA domains and the lipid polar head groups as well as the lipid aliphatic chains. All three simulations converged to a common binding interface, primarily involving interactions of the POTRA arm with the bilayer through the POTRA-1 domain, followed by the POTRA-2 domain. However, minimal interactions occurred between the POTRA-3 domain and the membrane. The predominant interactions between the POTRA-1/2 domains and the membrane bilayer were essentially mediated by lipid polar heads. Notably, specific residues, such as Arg31, Lys40, Lys88, Lys94, and Arg106 from POTRA-1 and Lys130 and Lys137 from POTRA-2, exhibited the highest relative contact times with lipid polar heads. This observation aligns with the involvement of lysine and arginine residues, which are frequently present in the coordination sphere of the phosphate moiety in protein/phospholipid complexes. Furthermore, a few residues also exhibited significant interactions with lipid aliphatic chains, including Arg31 and Ala35 from POTRA-1 and Lys130 from POTRA-2, which exhibited the highest relative contact times with lipid aliphatic chains.

TamA POTRA Domains Interact with Lipid Membranes. To investigate the putative interaction between the inner surface of the OM and the POTRA domains, we performed microscale thermophoresis (MST) experiments to measure the binding affinities between soluble POTRA constructs and calibrated liposomes as a lipid bilayer model. To mimic the bacterial membrane, we generated fluorescently labeled liposomes composed of polar lipid extracts of *E. coli* (composed of 65.3% PE, 22.6% PG, and 9.8% cardiolipin) and 2.5% 1,2-dioleoyl-sn-glycerol-3-phosphoethanolamine-N-(cyanine 5) or Cy5-PE (C18:1) as a fluorescent label (Fig. 4*A*). The purity and homogeneity of the vesicular membrane model were confirmed using a nanoparticle tracking analyzer on 100 nm-long extruded liposomes (Fig. 4*B* and *SI Appendix*, Fig. S4). A series of POTRA domain constructs were engineered to investigate the binding contributions of individual domains. POTRA-1, POTRA-2/3, and POTRA-1/2/3 were successfully expressed and purified with high yields of pure protein. However, the expression of the POTRA-2, POTRA-3, and POTRA-1/2 domains led to the formation of inclusion bodies; thus, these proteins were not included in the binding assay. Fig. 4*E* shows the direct associations between POTRA domains and vesicle membranes, with dissociation constants in the range of 3.09, 0.36, and 0.47 μM for POTRA-1/2/3, POTRA-1, and POTRA-2/3, respectively. To validate the binding interface predicted by MD simulations, we selected seven amino acids with a high residency time at the membrane surface, for which we anticipated that point mutations would decrease or abrogate membrane interactions (Fig. 4*C* and *SI Appendix*, Fig. S5). These seven lysine and arginine residues (R31, K40, K88, K94, R106, K130, and K137) are located on the POTRA-1/2 domains. The alanine mutant construct (mut-POTRA-1/2/3) was subsequently produced and purified to homogeneity and evaluated by binding titration assays via MST. In agreement with our MD simulation models, the septuple alanine mutations introduced at the predicted lipid interface displace the binding equilibrium, resulting in a significant loss of binding while retaining nearly identical stability properties compared to those of the wild-type POTRA-1/2/3 domain (Fig. 4 *D* and *E*). Although the mutated protein displays residual membrane-binding activity (two or more orders of magnitude lower), its dissociation constant could not be precisely determined because the titration reached the maximum solubility threshold for the protein. Taken together, these results confirm the membrane association of the POTRA arm, as predicted by the MD simulations, which establishes POTRA-1 and -2 as peripheral membrane domains. Accordingly, the liposome

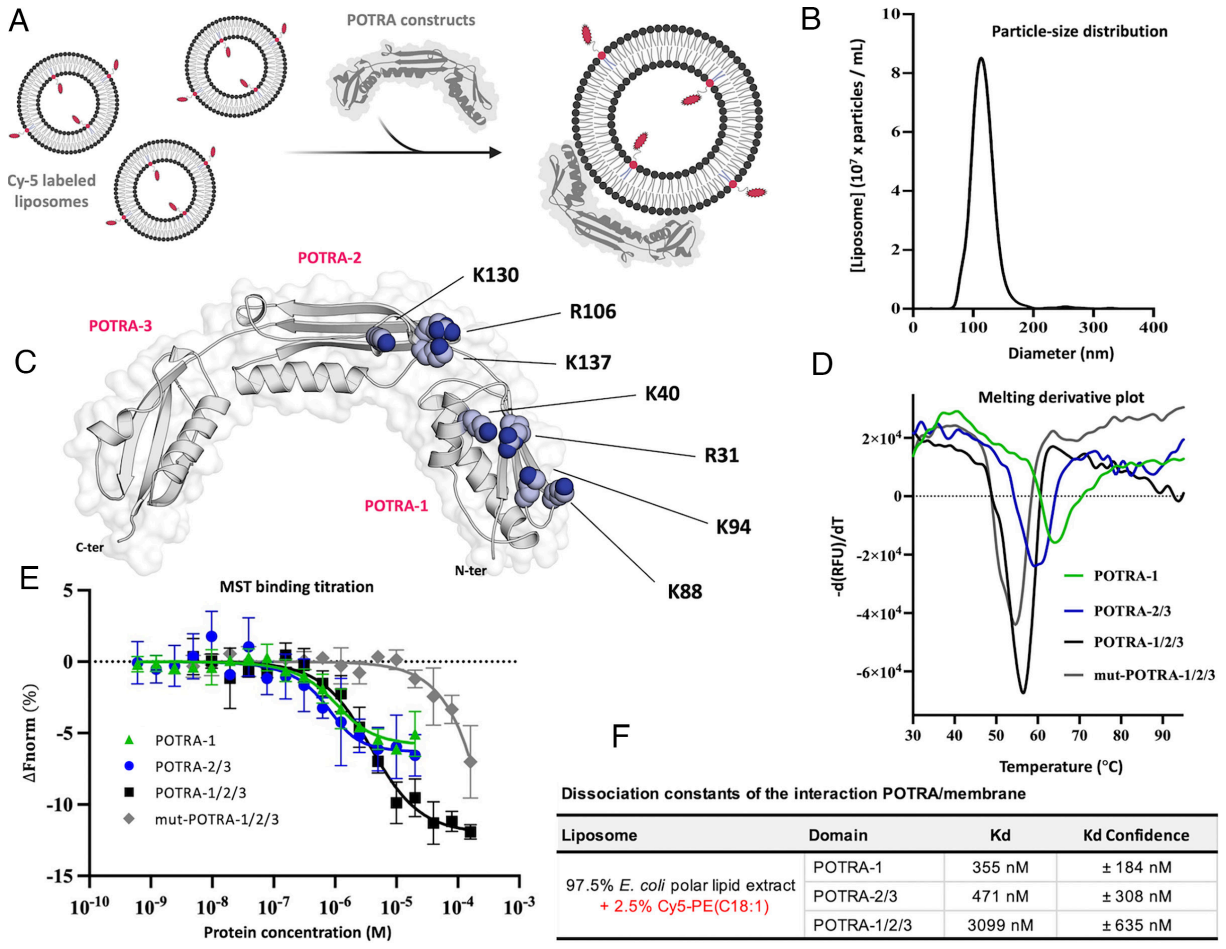

Dissociation constants of the interaction POTRA/membrane

Liposome	Domain	Kd	Kd Confidence
97.5% *E. coli* polar lipid extract + 2.5% Cy5-PE(C18:1)	POTRA-1	355 nM	± 184 nM
	POTRA-2/3	471 nM	± 308 nM
	POTRA-1/2/3	3099 nM	± 635 nM

Fig. 4. The POTRA arm of TamA binds to liposomes via a series of polar amino acids. (*A*) Cy5-labeled liposomes composed of 97.5% *E. coli* polar lipid extract (67% PE, 23.3% PG, and 9.7% cardiolipin) and 2.5% Cy5-PE(C18:1) phospholipids were used as a membrane model to study POTRA/membrane interactions. The liposomes were titrated with increasing concentrations of POTRA domains (mut-POTRA-1/2/3, POTRA-1/2/3, POTRA-2/3, and POTRA-1), and the dissociation constants were measured by MST. (*B*) Size distribution of the Cy5-labeled liposomes as determined with a particle tracking analyzer to confirm the homogeneity of the liposome samples. (*C*) Visual depiction of mutated amino acid positions at the predicted membrane interface. The POTRA arm is drawn in cartoon representation, whereas the side chains of the mutated residues are shown as spheres. (*D*) Derivative melt curve plots illustrating the thermostability of the POTRA-1, POTRA-2/3, POTRA-1/2/3, and mut-POTRA-1/2/3 domains as determined by DSF; the calculated melting temperatures are 64 °C, 61 °C, 55 °C, and 53 °C, respectively. (*E*) Dose–response curves for the binding interactions between Cy5-labeled liposomes and the POTRA-1 (green), POTRA-2/3 (blue), POTRA-1/2/3 (black), and mut-POTRA-1/2/3 (gray). The estimated K_d values are shown in panel (*F*).

binding assay identified POTRA-1 as the main attraction force, with contributions from POTRA-2, as suggested by the reduced membrane interaction observed with the septuple alanine mutant, wherein the putative binding interface is compromised.

Considering the variety of phospholipids populating the OM, the interaction between the POTRA domains and the membrane could favor a certain type of phospholipid. To determine the preferences of the POTRA domains, we formulated alternative liposome compositions to assess the individual contributions of specific phospholipid polar head groups according to their intrinsic physicochemical properties. Unfortunately, these liposome formulations enriched in phosphatidylethanolamine (PE) or PG were unstable in the presence of Cy5-PE (C18:1). Hence, we introduced up to 80% phosphatidylcholine (virtually absent in prokaryotic membranes) in our formulation because it is a generic component facilitating the formation of lipid vesicles; however, these liposomes still exhibited substantial heterogeneity, which made them noncompliant with MST (*SI Appendix*, Fig. S4). To overcome incompatibility issues in lipid formulation, a monolayer membrane model was used to investigate the specific contribution of phospholipids at the POTRA/membrane interface.

TamA POTRA Domains Selectively Interact with Unsaturated PE and PG Lipids. The Langmuir monolayer model serves as a versatile tool for emulating a physiological cell membrane by generating a membrane leaflet with comparable mechanical and thermodynamic properties (30, 31). This model is particularly well suited for mimicking the intricate environment of the inner leaflet due to the asymmetrical distribution of lipids within the OM. It allows for the creation of homogeneous and planar lipid membranes while affording control over a spectrum of parameters encompassing lipid composition, physical states, subphase constituents, pH, temperature, and surface tension (32). In this study, a variety of phospholipids were used, comprising zwitterionic PE lipids such as DPPE (*di*C16:0 PE) and DOPE (*di*C18:1 PE), as well as negatively charged PG lipids including DPPG (*di*C16:0 PG) and DOPG (*di*C18:1 PG). These choices were deliberately made to accurately mirror the native composition of the inner leaflet in the OM of gram-negative bacteria (33). They were also chosen for their ability to represent a range of characteristics that influence protein–membrane interactions, such as the size and charge of the polar head, the length of the acyl chain, and the degree of unsaturation, all of which impact the physical properties of the membrane (34).

We probed the interactions of the POTRA-1, POTRA-2/3, and POTRA-1/2/3 constructs with saturated DPPE and DPPG lipids under ordered gel phase conditions (the phase transition temperatures of DPPE and DPPG are 63 °C and 41 °C, respectively). We observed comparable maximum insertion pressure (MIP) values at saturating protein concentrations with a predilection for zwitterionic DPPE lipids (approximately 38 and 32 mN/m for DPPE and DPPG lipids, respectively) (Fig. 5 and *SI Appendix*, Fig. S6). These interactions with the membrane were associated with higher synergy values for the POTRA-2/3 and POTRA-1/2/3 domains. In contrast, when testing unsaturated DOPE and DOPG lipids, POTRA-1 consistently exhibited higher MIP values than did POTRA-2/3 and POTRA-1/2/3 (42 and 53 mN/M for DOPE and DOPG, respectively), with notably high synergy values above 0.5 toward DOPG. Collectively, these results underscore the binding preference of the POTRA domains for associating with lipids in disordered liquid crystalline phase membranes (the phase transition temperatures of DOPE and DOPG are −16 °C and −18 °C, respectively), which more accurately represents the natural state of biological membranes. These interactions are dominated by the strong affinity between the POTRA-1 domain and PG head groups in the disordered membrane, as indicated by the large MIP and synergy values of POTRA-1 and DOPG, which exceeded 50 mN/m and 0.5, respectively (*SI Appendix*, Fig. S6). This strong interaction might conceivably denote physiological significance, given that PG constitutes the second most prevalent constituent (~20%) of the inner leaflet following PE (~75%) (35). Moreover, the PG lipids have been previously demonstrated to facilitate OMP assembly over PE lipids in a liposome model (36, 37).

In the presence of mixed lipid membranes composed of a POPE/POPG mixture (80/20 ratio) or *E. coli* polar lipids, the MIP values of all three constructs were comparable. However, the three constructs demonstrated a greater preference for the POPE/POPG mixture than for the *E. coli* membrane extract, substantiated by their higher MIP and synergy values (Fig. 5*A* and *SI Appendix*, Fig. S6). This phenomenon can be attributed to the composition of the polar lipids in *E. coli*, which comprise blends of lipids from both the outer and inner membranes. This is different from the POPE/POPG mixture, which closely mimics the inner leaflet of the OM. These observations support earlier observations, in which the POTRA-1 domain predominantly influenced the MIP values, while the POTRA-2/3 domains primarily contributed to the synergy values. This finding suggests that POTRA-1 is engaged in membrane binding, whereas the POTRA-2/3 arm participates in enhancing membrane affinity, positioning itself in closer proximity to the membrane prior to consolidating interactions with POTRA-1.

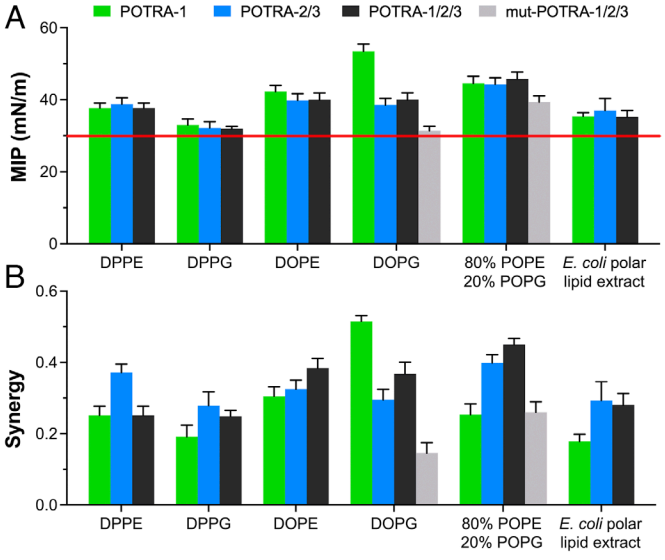

Fig. 5. POTRA-1 preferentially interacts with unsaturated PG lipids. Histogram plot showing the MIP values (*A*) and synergy values (*B*) of POTRA-1, POTRA-2/3, POTRA-1/2/3, and mut-POTRA-1/2/3 for six phospholipids composed of DPPE (diC16:0 PE), DPPG (diC16:0 PG), DOPE (diC18:1 PE), DOPG (diC18:1 PG), POPE (C16:0 C18:1 PE), POPG (C16:0 C18:1 PG), and *E. coli* polar lipid extract. A MIP value below 30 mN/m (representing the physiological membrane pressure) indicates a lack of interaction with the monolayer.

To corroborate and cross-validate the identification of the lipid binding interface on the POTRA-1/2 region, we introduced the septuple mutant mut-POTRA-1/2/3 and evaluated its interactions with DOPG and POPE/POPG membranes. The mutations resulted in a substantial reduction in both the MIP and synergy values when compared to those of the wild-type POTRA-1/2/3 construct (Fig. 5 and *SI Appendix*, Fig. S6). This outcome aligns with our MD and MST data, reinforcing the pivotal role of the mutated amino acids (R31, K40, K88, K94, R106, K130, and K137) in facilitating the interaction between the POTRA domains and the membrane.

The TamA POTRA Domain Modulates Lipid Bilayer Properties. In contrast to conventional protein–protein interactions, protein–membrane surface interactions represent a relatively unexplored domain, owing to technical challenges that need to be surmounted. Nonetheless, the limited studies conducted in this area, particularly regarding peripheral membrane proteins, provide evidence that protein interactions can locally modulate the physical and dynamic properties of the membrane (38–40). To explore the impact of POTRA/membrane interactions on global bilayer equilibrium, we evaluated membrane fluidity by measuring the phase transition temperature (Tm) of the membrane in the presence and absence of different POTRA constructs. For this purpose, we used a Laurdan fluorescent probe, which emits varying signals depending on whether the lipid phase state is in a gel or liquid form (41), exhibiting blue-shifted fluorescence when lipids are in a more packed phase (Fig. 6). For this assay, we selected DMPG (*di*C14:0 PG) and POPE (C16:0-C18:1 PE) lipids because their phase transition temperatures (23 °C and 25 °C, respectively) fall within the measurable range of our experimental setup; furthermore, both PG and PE lipid membranes associate with the POTRA arm (Fig. 5). In the absence of the POTRA arm, the measured Tm values aligned with the Tm values documented in the literature for pure DMPG membranes at 23 °C (Fig. 6 *A* and *B*). However, when DMPG liposomes were incubated with PG-interacting POTRA constructs (POTRA-1, POTRA-2/3, and POTRA-1/2/3), a 1 °C increase was consistently observed, indicating that the POTRA domain contributes to the physical stabilization of the lipid bilayer. This stabilization was not observed for the POPE membranes (Fig. 6 *C* and *D*). Interestingly, the septuple mutant (mut-POTRA-1/2/3), which possesses a reduced membrane binding affinity, had no influence on membrane fluidity. This observation suggests that the stabilization of the DMPG bilayer is specifically dependent on the binding interface with a functional POTRA domain. The decrease in membrane fluidity for DMPG can be attributed to the restricted lateral diffusion of PG, arising from interactions with the POTRA domain. This binding interaction with PG lipids, along with their constrained diffusion, is likely to sustain a localized enrichment of PG lipids near the lateral gate. This accumulation is anticipated to promote a more conducive environment for OMP folding, given the positive correlation between OMP assembly and the accumulation of PG and the

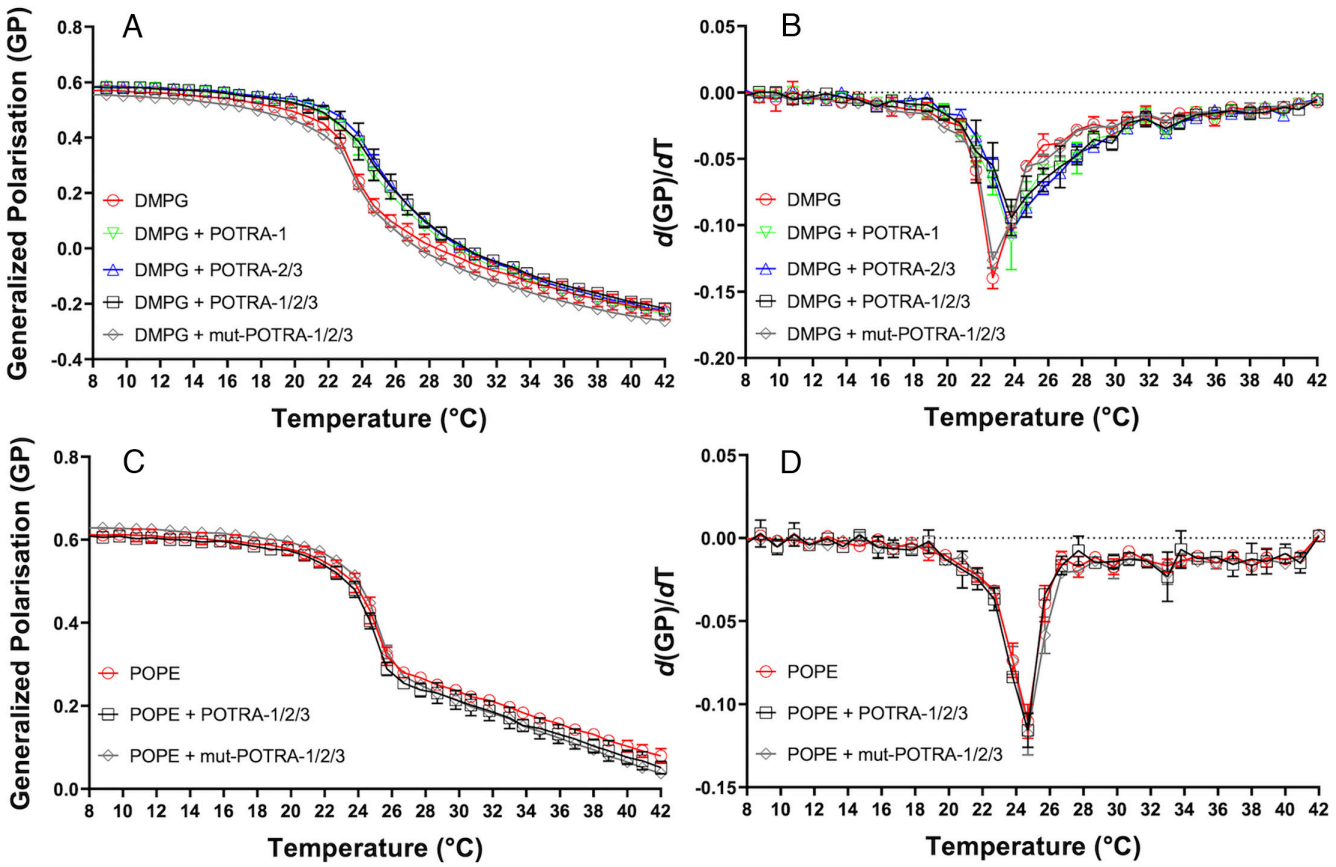

Fig. 6. The POTRA arm binds to DMPG lipids and increases their phase transition temperature. Global phase transition temperature assessment for DMPG and POPE vesicle membranes, alone (red) or in the presence of POTRA-1 (green), POTRA-2/3 (blue), POTRA-1/2/3 (black), or mut-POTRA-1/2/3 (gray) by the Laurdan fluorescence assay. (*A*) GP values as a function of temperature in DMPG membranes. (*B*) The first derivative of the GP curves illustrates the phase transition temperature (Tm) of DMPG membranes at the peak values. The calculated Tm values are 23 °C for liposomes alone or with mut-POTRA-1/2/3, and 24 °C for liposomes with POTRA-1, POTRA-2/3, and POTRA-1/2/3. (*C*) GP values as a function of temperature for the POPE membranes. (*D*) The first derivative of the GP curves illustrates the phase Tm of POPE liposomes at the peak values. The calculated Tm values are 24 °C for liposomes alone or in the presence of POTRA-1/2/3 or mut-POTRA-1/2/3.

local distribution of negative charges across the membrane (LPS and PG), which collectively contribute to lowering the kinetic barrier for OMP assembly (36, 37, 42).

Discussion

In gram-negative bacteria, the catalytic units BamA and TamA play pivotal roles in the insertion and assembly of β-barrel OMPs. These processes occur through parallel pathways denoted as BAM and TAM, respectively. Both BamA and TamA are members of the OMP85 family of proteins; they share strong structural similarity in terms of their β-barrel configuration and are thought to function via a conserved gating mechanism. While TamA is not essential, it is nonetheless vital for preserving membrane integrity and orchestrating the assembly of specific virulence factors. Notably, the deletion of *tamA* in multidrug-resistant pathogens such as *Klebsiella pneumoniae* and *Edwardsiella tarda* results in increased antibiotic susceptibility and diminished virulence (13). Considering the significance of TamA in pathogenic species, the translocation and assembly module has emerged as a pertinent candidate for the development of anti-infective agents, thereby emphasizing the imperative need to unravel its intricate molecular mechanism (3, 7, 13).

To further understand how TamA operates, particularly within infectious microorganisms, we solved its crystal structure from a pathogenic *P. aeruginosa* strain in three distinct conformations. These structures illustrate the dynamic nature of the POTRA domains, operating as a rigid lever arm capable of considerable vertical motion (Fig. 2). These structural observations are consistent with preceding magnetic contrast neutron reflectometry data, pointing to the existence of two extreme lever-arm conformers upon substrate binding to TamA (12, 28). However, the identification of the inflection point had been purely speculative and lacked experimental confirmation before this study. This transformation within the protein's conformational landscape is notably facilitated by the flexible junction between the β-barrel and POTRA-3 domains, allowing the POTRA arm to move toward or away from the OM. This association with the membrane was not initially observed in the *Ec*TamA structure, as the POTRAs were constrained to an extended conformation within the crystal lattice (15). Using MD simulations, we further explored the behavior of *Pa*TamA, confirming the ability of the POTRA domains to approach the membrane closely and engage with lipid headgroups through a series of polar amino acids lining the POTRA-1 and POTRA-2 domains (Fig. 3). To validate these predictions, we quantified the dissociation constant between lipid vesicles (*E. coli* lipids) and various POTRA constructs, revealing binding events within the nanomolar range. Moreover, these interactions were corroborated in a lipid monolayer model, demonstrating the versatile capacity of the POTRA arm to interact with curved and flat membrane surfaces (Figs. 4 and 5). The insights gained from the MD simulations were instrumental in pinpointing the interface responsible for membrane binding, as well as delineating the amino

acids within POTRA-1 and POTRA-2 responsible for mediating adhesion with the inner leaflet of the OM. Accordingly, mutations in these amino acids (R31/K40/K88/K94/R106/K130/K137) led to a marked reduction in binding affinity, as evidenced by both monolayer and bilayer membrane models, confirming their importance in maintaining interactions with the bacterial membrane. Considering the relevance of arginine and lysine residues for the POTRA–membrane interaction, we examined their conservation in the *Ec*TamA structure. This analysis corroborates our observations of a basic surface, composed of lysine and arginine residues, at the membrane interface (12, 43). Although *Ec*TamA and *Pa*TamA share a similar pattern of positive charges within their membrane-binding site, the positions of these residues vary among TamA orthologs, yet preserving local surface properties (*SI Appendix*, Fig. S7). Such variations are frequently observed in peripheral membrane proteins (43) and probably arise from evolutionary adaptations to differing environmental conditions, where bacterial lipid compositions may vary in response to specific ecological niches or envelope stresses (33, 44).

The periplasmic leaflet of the OM in gram-negative bacteria primarily consists of PE and PG lipids which have various degrees of unsaturation and acyl chain length (33, 45). Our monolayer interaction study showed that the different POTRA domains interact with both zwitterionic and negatively charged lipid surfaces, comprising PE and PG. However, these interactions are notably enhanced in the presence of unsaturated PG, which has the highest affinity for POTRA-1 under all tested conditions (Fig. 5). Our working model is that PG lipids, present as a minor component of the inner leaflet (~20% PG vs. ~75% PE) (35), tend to accumulate locally at the POTRA/membrane interface due to their higher affinity over PE. Considering the zwitterionic nature of PE and the negative charge of PG, this preference can be attributed to complementary charges between Arg/Lys residues and the PG lipids. Accordingly, this interaction depends on the presence of arginine and lysine residues, as demonstrated by the reduced PIM and synergy values observed in the mut-POTRA1/2/3. These findings are illustrated in Fig. 5, using DOPG membrane in the physiological liquid crystalline phase, and supported by the inability of the septuple Arg/Lys mutant to influence the phase transition of PG membranes toward a higher ordered state when compared to the wild type constructs (Fig. 6*B*).

This binding preference suggests that POTRA domains effectively recruit unsaturated phospholipids around the β-barrel lateral gate, favoring PG lipids (Fig. 5), which have been shown to positively influence OMP assembly over PE lipids (36, 37, 42). Conversely, PE, a major constituent of bacterial membranes, exerts inhibitory effects, impeding OMP assembly in liposome membrane models (37). This concept is supported by the ability of the POTRA domains to interact with and restrict the diffusion of PG lipids at their binding interface, substantiating the idea that the POTRA domains reconfigure the lipid distribution near the lateral gate in favor of PG (Fig. 6). Moreover, in the context of densely populated membranes, periplasmic POTRA domains can serve as a steric exclusion mechanism to facilitate lipid accessibility for the insertion of nascent proteins into an environment congested with existing OMPs (5, 27).

Building upon our findings and recent research on the BAM and TAM chaperones, we present a refined functional model of the TAM machinery (Fig. 7). In this model, the POTRA arm assumes a crucial role in regulating TamA insertase function by interacting with the membrane surface, thereby influencing the local properties of the OM and facilitating OMP assembly. Briefly, in its resting conformation, the POTRA arm associates with the outer membrane, promoting the local enrichment of PG lipids near the β-barrel active site (Fig. 7*A*). This interaction excludes existing OMPs, ensuring membrane availability for the insertion of incoming OMP clients. Upon interaction with the protein substrate, the POTRA arm dissociates from the membrane (28). The conformational change in TamA is expected to either cause bending in TamB or induce TamA to exert pressure against the OM, resulting in localized membrane distortion. The latter hypothesis is more widely accepted due to the rigidity of the peptidoglycan layer, which would prevent TamB from undergoing lateral shifting or bending (9, 12, 28)

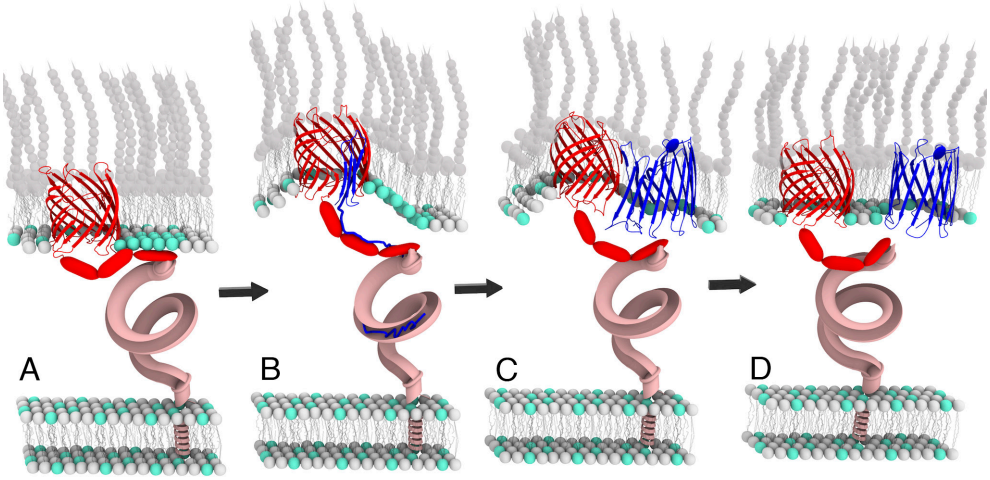

Fig. 7. Refined functional model of the TAM machinery. (*A*) The TAM machinery is composed of the inner membrane protein TamB (depicted in pink, resembling a spiral conduit based on its AlphaFold structural prediction) and TamA (depicted in red, shown in cartoon representation), which act as a periplasmic ladder and an OMP insertase, respectively (7, 47). The TAM is held together through interactions between the carboxy terminus of TamB and the POTRA-1 domain of TamA (7). In its resting conformation, the POTRA arm associates with the outer membrane, participating in the local accumulation of PG lipids (green spheres) in the nearby environment of the lateral gate. The local distribution of negative charges across the membrane (LPS in the outer leaflet and PG in the inner leaflet) positively influences OMP folding (36, 37, 42). The membrane-bound POTRA domains also contribute to steric interactions with existing OMP, ensuring lipid accessibility for the insertion of nascent proteins (27). (*B*) TamB functions as a delivery conduit to transport nascent OMPs and glycerophospholipids across the periplasm and peptidoglycan layer (not represented to simplify the model) (47–49). The interaction with the OMP substrate (blue) triggers conformational changes within TamA, characterized by the opening of the lateral gate (18) and the vertical displacement of the POTRA arm away from the outer membrane (28). This structural transition results in local outer membrane distortion and lipid perturbation, in favor of OMP assembly. (*C*) Within the lateral gate of TamA, strand β1 acts as a seeding template mediating the binding of the C-terminal β-strand motif of the substrate, assembling the nascent OMP by sequential β-augmentation, proceeding from the C terminus to the N terminus, generating a hybrid barrel (20). (*D*) This process continues until the fully assembled OMP is eventually released, a step that could be potentially facilitated by the reassociation of the POTRA domains with the outer membrane, fostering steric interaction with the newly assembled OMP.

(Fig. 7*B*). The lever arm movement likely imposes structural tensions on the β-barrel due to the direct connection of the articulated POTRA arm to the β-barrel's lateral gate (Fig. 1*A*). This contributes to the gating mechanism that catalyzes the assembly of the OMP client, akin to the process observed in BamA, where a transient hybrid barrel forms at the lateral gate (19, 20) (Fig. 7*C*). Although the hybrid barrel intermediate has not been directly confirmed in TamA, it is inferred based on its strong structural homology with the β-barrel of BamA (15). This homology encompasses an atypical lateral gate conserved in BamA and TamA (15, 46) (Fig. 1), which has been demonstrated in BamA to trigger the assembly of OMP clients through the growth of a transient hybrid barrel by sequential β-augmentations (20–22). This cycle progresses until the release of the newly folded protein, followed by the reattachment of TamA POTRAs to the membrane in the resting conformation (Fig. 7*D*).

An intriguing question persists in the functional model of the lipidated TamL variant, as it is less likely that the POTRA will dissociate from the membrane due to the membrane-anchored POTRA-1 domain. An alternative model for TamL may involve alternating the vertical POTRA motion through rotational movement (along the membrane plane) upon substrate binding to regulate the gating activity of the catalytic site. Alternatively, this variant might heavily rely on membrane modification to facilitate OMP assembly, or it could primarily function to maintain TamB near the outer membrane, facilitating TamB-dependent lipid transport across the inner and outer membranes in the *Bacteroidetes* and *Chlorobiota* phyla (48, 49). Additional experiments will be required to refine the current TAM model, especially to unravel the elements controlling the lateral gate of TamA. This will necessitate further exploration through the capture of intermediary conformational states of TAM via X-ray crystallography or cryoelectron microscopy.

Materials and Methods

Materials. The buffer solutions were prepared using deionized water obtained from a Barnstead Nanopure system (Dubuque, IA). The resistivity and surface tension of the water at 20 °C were 18.2 MΩ cm and 72 mN/m, respectively. Tris (Base) and butylated hydroxytoluene were purchased from Fisher Scientific (Hampton, NH), hydrochloric acid was obtained from VWR International (Radnor, PA), and potassium phosphate monobasic acid was obtained from VWR International (Radnor, PA). High-performance liquid chromatography–grade chloroform and methanol were acquired from Laboratoire Mat (Quebec, Canada). The phospholipids and *E. coli* Polar Lipid Extract used in the study were obtained from MilliporeSigma (Burlington, MA). The lipid solutions were prepared in chloroform at 20 mg/mL and stored at −20 °C. Unsaturated lipids were kept under an argon atmosphere with 5 μg/mL of the antioxidant butylated hydroxytoluene, while saturated lipids were stored under atmospheric air.

Plasmid Cloning. Cloning in this study was performed using the restriction-free cloning method (50). Briefly, the coding sequence of the predicted mature TamA protein from *P. aeruginosa* PAO1 (*Pa*TamA$_{25\text{-}579}$) was cloned between the BamH1 and Xho1 endonuclease sites of a modified pET20 expression plasmid and downstream of the PelB signal sequence, hexahistidine tag, and TEV cleavage site. The POTRA domain constructs POTRA-1/2/3 (*Pa*TamA$_{25\text{-}270}$), POTRA-2/3 (*Pa*TamA$_{105\text{-}270}$), and POTRA-1 (*Pa*TamA$_{25\text{-}104}$) were cloned and inserted into a pNIC-CTHF vector upstream of a hexahistidine tag and a TEV cleavage site using the same approach. Site-directed mutagenesis was performed using the whole-plasmid PCR mutagenesis method (51). Briefly, the pNIC-CTHF-POTRA-1/2/3 plasmid was amplified with a pair of complementary oligonucleotides encoding a selected mutation. After 18 amplification cycles, the methylated parental plasmids were digested by the addition of 10 units of DpnI for 15 min, and the PCR mixture was transformed into *E. coli* SIG10 competent cells prior to selection on LB agar supplemented with 50 μg/mL kanamycin. Individual colonies were grown in 5 mL of LB media overnight and the plasmids were purified using a QIAGEN miniprep kit prior to Sanger sequencing to confirm the introduction of the desired mutation. The procedure was reiterated for the accumulation of additional mutations. The plasmids and oligonucleotides used in this study are listed in *SI Appendix*, Table S1.

Expression and Purification. Chemically competent *E. coli* BL21 (λ DE3) C43 cells were transformed with the *Pa*TamA$_{25\text{-}579}$ expression plasmid by heat shock. Cells containing the plasmid of interest were selected by plating on LB agar in the presence of ampicillin. After the cells had grown in 2YT medium at 37 °C to an OD_{600nm} of 1, the temperature was decreased to 30 °C, and the expression of *Pa*TamA was induced with 0.5 mM IPTG. After 16 h of expression, the *E. coli* cells were harvested at 6,000 rpm for 15 min and resuspended in cold lysis buffer [20 mM HEPES pH 8, 0.2 M NaCl, 1% (w/v) Elugent (Calbiochem), DNase I, $MgCl_2$, lysozyme, and PMSF] and then lysed by sonication. Cell debris and unbroken cells were pelleted by centrifugation at 16,000 rpm for 1 h, and the supernatant containing solubilized TamA was incubated for 1 h with 5 mL of Ni-NTA resin under gentle agitation at 4 °C. The bound His_6-tagged TamA was eluted with step gradients ranging from 20 mM to 500 mM imidazole in a mobile phase composed of 20 mM HEPES (pH8), 0.2 M NaCl, and 0.5% (w/v) C_8E_4. The protein fractions were pooled and digested with TEV protease at 4 °C overnight. TamA was concentrated to 10 mg/mL and subsequently gel-filtered on a Superdex 200 column (GE Healthcare) in 20 mM HEPES pH 8, 0.2 M NaCl, and 0.5% (w/v) C_8E_4. The selenomethionine-labeled *Pa*TamA$_{25\text{-}579}$ was expressed using the methionine auxotrophic *E. coli* BL21 (DE3) B834 strain cultured in autoinducible minimal media 5052 supplemented with selenomethionine and was ultimately purified following the same protocol as the native protein. The four POTRA domain constructs, POTRA-1, POTRA-2/3, POTRA-1/2/3, and mut-POTRA-1/2/3 were overexpressed in *E. coli* BL21 (λ DE3) in LB media. Bacteria were grown at 37 °C to an OD_{600nm} of 0.8, prior to overnight protein induction with 0.5 mM IPTG at 22 °C. The cells were harvested by centrifugation and lysed in 20 mM HEPES pH 8, 0.2 M NaCl, DNase I, $MgCl_2$, lysozyme, and PMSF. The soluble POTRA domains were purified with the same method as described above except for the use of mobile phase buffers that contained no detergent. The identity and purity of the protein samples were evaluated by mass spectrometry and SDS-PAGE analysis.

TamA Structure Determination. The native and seleno-Met derivative *Pa*TamA$_{25\text{-}579}$ were concentrated to 10 to 15 mg/mL using a 100 kDa cutoff centrifugal concentration device. The crystallization was done using the sitting-drop vapor diffusion method with a ratio of protein solution to the reservoir of 1:1. Four conditions yielding diffracting-quality crystals in space groups $C222_1$ (60% hexylene glycol and 0.1 M HEPES pH 7.4), $P2_1$ (12% peg 4 K, 50 mM $MgCl_2$, 70 mM HEPES pH 7.2, 4% isopropanol, and 10% glycerol), C2 (11% peg 3350, 0.1 M magnesium formate, and 70 mM sodium cacodylate pH 6.0), and $P22_12_1$ (18% peg 3350, 0.2 M NaI, and 0.1 M HEPES pH 8.0) were optimized from multiple hits obtained from the JCSG+, index, and MCSG1-4 crystallization suites. A partial solution was obtained via the molecular replacement method using the β-barrel domain from *Ec*TamA (PDB code 4C00) as search models in the $P2_1$ native crystal form, which diffracted to 2.9 Å resolution. A complete model covering the full-length sequence of *Pa*TamA$_{25\text{-}579}$ was ultimately built using our partial solution model and experimental phases obtained from a $P2_1$ selenomethionine-derivative crystal collected to 2.6 Å resolution at the selenium edge. This final model was used to solve all other crystal forms of *Pa*TamA using molecular replacement. In the $C222_1$ crystals only the TamA β-barrel domain was present due to proteolytic cleavage (the $C222_1$ crystal form appeared after 4 mo at 20 °C). The Phenix suite and Coot (52, 53) software were used during structure determination, refinement, and building cycles. The unit cell dimensions and refinement statistics are summarized in *SI Appendix*, Table S2.

MDs Simulations. The amino acid sequence of TamA from *P. aeruginosa* (residues 25 to 579) and coordinates were obtained from the PDB entry 8US2 chain A (solved in this study). The structure was validated, and hydrogens were added with MolProbity (54). The position of TamA in the membranes was predicted using the PPM 2.0 server (55), and the POTRA-1 (residues 25 to 104) and POTRA-2 (residues 105 to 189) segments were manually placed at a distance of at least 20 Å from the membrane surface. The CHARMM-GUI Membrane Builder (56, 57) was used to embed TamA in a POPE:POPG (80:20) bilayer, with 200 lipids per leaflet, for a total of 400 lipids and more than 50,000 water molecules. All the ionizable residues were considered to be in their standard protonation state at pH 7. The default N-terminal and C-terminal patches were used. The system was

neutralized to an ionic concentration of 0.15 mM using NaCl. The simulations were performed with the NAMD 2.14 program (58) using the CHARMM36m force field (59) and TIP3P waters (60, 61). Simulations were carried out at 303.15 K under isothermal–isobaric (NPT) ensemble conditions with a 2-fs time step and periodic boundary conditions. Langevin damping with a coefficient of 1 ps−1 was used to maintain a constant temperature, while the pressure was controlled by a Nosé-Hoover Langevin piston at 1 atm. The length of the bonds between hydrogen and heavy atoms was constrained using SETTLE (62) for water molecules and SHAKE (63) for all other molecules. The cutoffs for short-range electrostatics and Lennard-Jones interactions were set at 12 Å, with the latter smoothed by a switching function over the range of 10 Å to 12 Å. Long-range electrostatic interactions were calculated with the particle mesh Ewald method (64, 65) using a sixth-order interpolation and a grid spacing of ≈1 Å at each integration step. The nonbonded pair lists were updated every 10 steps, and the coordinates were saved every 10 ps for analysis. Three 1-μs trajectories were produced, and the last 300 ns of each trajectory were used for analysis. The coordinates were saved every 10 ps for analysis. The relative contact times between the POTRA-1/2/3 residues and the lipid polar heads, and between the POTRA-1/2/3 residues and the lipid aliphatic chains, were considered. The relative time of contact was defined as the fraction of frames of the trajectories in which a contact between any heavy atom from a residue of POTRA-1/2/3 was within a distance of 4 Å of at least one heavy atom of one of the chemical groups of lipids. The lipid polar head atoms were defined as any heavy atoms of the PG or PE groups of the POPG or POPE lipids, respectively. Atoms of the lipid aliphatic chains comprised carbons from the second position of the acyl chain and beyond. Distances were calculated using WORDOM software (66).

Preparation and Analysis of Fluorescently Labeled Liposomes. Liposomes were formed from a total of 0.5 mmol of lipids composed of 97.5% *E. coli* polar lipid extracts and 2.5% Cy5-PE (C18:1) prepared in a glass tube. A uniform lipid film was created by evaporating the chloroform solution under a stream of nitrogen gas. After drying in a vacuum desiccator overnight, the lipid film was resuspended in 20 mM HEPES (pH 8) and 0.2 M NaCl to a final concentration of 0.5 mM. The lipid suspension was extruded 12 times through a 0.1 μm polycarbonate membrane to generate calibrated unilamellar vesicles of 100 nm. Liposomes were freshly prepared before each MST experiment. The size, homogeneity, and concentration of the lipidic vesicles were determined using a nanoparticle tracking analyzer. Analyses were performed with a Nanosight NS3000 (Malvern) at a 1:2,000 dilution in 20 mM HEPES (pH 8), 0.2 M NaCl, and 0.05% Tween 20, yielding 40 to 80 particles/frame. The samples were injected according to the following settings: camera level: 15, data collection: 3 × 60 s, flow rate: 75 μL min^{-1}, and analysis setting: 6 to 8. The data were recorded in triplicate, and the videos were analyzed with nanoparticle tracking analysis (NTA) 2.0 software.

MST Assay. POTRA-1/2/3 and mut-POTRA-1/2/3 were prepared at 320 μM, and POTRA-2/3 and POTRA-1 were prepared at 80 μM. From these stock solutions, twofold serial dilutions were carried out to generate sixteen samples. The labeled liposomes were diluted 200-fold in 20 mM HEPES (pH 8), 0.2 M NaCl, and 0.01% Tween 20 to a final lipid concentration of 2 μM. Following dilution, the liposomes were immediately mixed in equal volumes with the 16 protein samples. The protein/liposome mixtures were loaded in capillaries to titrate the binding association between fluorescently labeled lipid vesicles and POTRA domains using a Monolith NT.115 instrument (NanoTemper, Germany). All the experiments were performed in triplicate using 2% MST power and laser on/off times of 20/5 s. Binding titration analyses were carried out using NanoTemper analysis software, and the dissociation constants were calculated using a simple 1-to-1 binding model according to the law of mass action (67).

Protein Adsorption Measurements in Monolayers. The surface pressure (π) was measured with a DeltaPi4 microtensiometer (Kibron Inc., Helsinki, Finland) using the Wilhelmy method in a 1,000 μL Teflon trough (diameter: 18 mm; depth: 5 mm). A Plexiglass box was used to regulate humidity during the experiments, and the temperature was maintained at 20 ± 1 °C. The subphase in the trough consisted of 1,000 μL buffer of 500 mM potassium phosphate monobasic buffer, 200 mM Tris-base, and 100 mM sodium chloride at pH 7.0. The saturating concentrations of the POTRA domain constructs were determined by injecting increasing volumes underneath the subphase surface, and the concentrations were found to be 121 μg/mL for POTRA-1, 202 μg/mL for POTRA-2/3, 322 μg/mL for POTRA-1/2/3, and 27 μg/mL for mut-POTRA-1/2/3 for respective surface pressure values of 11, 23, 20, and 22 mN/m, which corresponded to the onset of monolayer saturation and were used for all subsequent experiments with the corresponding constructions. To conduct the experiments, a few microliters of the phospholipid solution were spread onto the subphase to achieve the desired initial surface pressure (πi). The film was then left until the spreading solvent evaporated completely and the film reached equilibrium; the time required depended on the lipid type, the spreading volume, and the initial surface pressure. The POTRA-1, POTRA-2/3, POTRA-1/2/3, and mut-POTRA-1/2/3 constructs were subsequently injected beneath the lipid monolayer at their respective saturating concentrations (see above), and the interaction between the four POTRA domain constructions and the phospholipid monolayer was monitored during the experiment with surface pressure kinetics until the equilibrium surface pressure (πe) was reached. The binding parameters were calculated following a previously described method, and the uncertainties were determined accordingly. To summarize, the change in surface pressure ($\Delta\pi = \pi e - \pi i$) resulting from protein injection was plotted as a function of the initial surface pressure (πi), and a linear regression was fitted to the data. The MIP was determined at the intersection of the plot with the x-axis, and the synergy was calculated by adding 1 to the slope. The uncertainty of the MIP was calculated from the covariance of the experimental data on the linear regression, while the uncertainty of the synergy was calculated using the formula $[\sigma(\pi e)\ (1 - r2)1/2]/[\sigma(\pi i)\ (n - 2)1/2]$, where σ denotes the SD, r denotes the correlation coefficient, and n denotes the number of data points. The calculations of the binding parameters and their uncertainties were performed using an online software calculator, which can be accessed at http://www.crchudequebec.ulaval.ca/BindingParametersCalculator/.

Protein Stability Assay by Differential Scanning Fluorescence (DSF). DSF was performed to assess protein stability by monitoring the thermal unfolding of the POTRA domains using the Protein Thermal Shift™Dye (Applied Biosystems™) as a probe. Briefly, 0.5 mg/mL of POTRA constructs were incubated with 1× SYPRO orange dye at a final concentration of 20 mM HEPES (pH 8), 200 mM NaCl, and 2% DMSO. The mixture was then immediately distributed into a 96-well microplate and heated from 25 °C to 99 °C at a rate of 0.05 °C/s using a StepOnePlus™ Real-Time PCR system (Applied Biosystems™). The fluorescence intensity was recorded using a ROX emission filter (645 nm), and melting curves were generated using StepOne Software by plotting the negative first-derivative normalized fluorescence as a function of the temperature.

Determination of the Lipid Phase Transition Temperature by Generalized Polarization (GP). Liposomes (0.2 mM of DMPG) were prepared as described above and incubated at room temperature for 1 h with 8 μM Laurdan fluorescent probe in a solution containing 20 mM HEPES (pH8), 200 mM NaCl, and 0.25% DMSO. Subsequently, POTRA constructs were added (or not) at a lipid/protein ratio of 1/400, and the mixture was heated from 8 °C to 42 °C using a Cary Eclipse Fluorescence Spectrometer (Agilent). As the temperature increased the fluorescence emission intensity was recorded at two wavelengths, 450 nm and 490 nm, with the excitation wavelength set at 360 nm. The GP was calculated as $GP = [(I_{450nm} - I_{490nm})/(I_{450nm} + I_{490nm})]$ and plotted against temperature (41); the transition temperature of the lipid vesicle membrane was determined from the first derivative of the curve. All the experiments were performed in triplicate.

Data, Materials, and Software Availability. Atomic coordinates for the crystal structures of *Pa*TamA have been deposited in the Protein Data Bank under the PDB entries 8US1, 8US2, 8US3, and 8US4 (68–71).

ACKNOWLEDGMENTS. We thank Jihen Ati (Institut National de la Recherche Scientifique, INRS), who contributed to the early phase of this study, and intern Marta Zdanovska (Institut National de la Recherche Scientifique, INRS), who provided technical assistance and express appreciation to Dr. Joseph Schrag (National Research Council of Canada) for reviewing and proofreading the manuscript. This work was supported by the Natural Sciences and Engineering Research Council of

Canada (NSERC) Discovery grant RGPIN-2017-06091 and RGPIN-2022-03958 as well as the PROTEO new collaborative initiatives program and new investigator grant 2019-NC-253753 from the Fonds de Recherche du Québec - Nature et Technologie. This research used synchrotron resources from the Canadin Light Source at Beamline 08ID-1, which is supported by the Canada Foundation for Innovation, NSERC, and Canadian Institutes of Health Research. We appreciate Compute Canada's support for the High Performance Computing platform, without which current MD simulations would not have been possible. E. Boisselier is a Junior 2 Research Scholar from the Fonds de Recherche du Québec - Santé. The funders had no role in the study design, data collection or interpretation, or the decision to submit the work for publication.

Author affiliations: [a]Institut National de la Rechyuerche Scientifique (INRS), Centre Armand-Frappier Santé Biotechnologie, Laval, QC H7V 1B7, Canada; [b]Regroupement Québécois de recherche sur la fonction, la structure et l'ingénierie des protéines (PROTEO), Université du Québec à Montréal, Montréal, QC H2X 3Y7, Canada; [c]Faculty of Medicine, Department of Ophthalmology and Otolaryngology—Head and Neck Surgery, centre hospitalier universitaire de Québec, Université Laval, Québec City, QC G1S 4L8, Canada; [d]Département de Biochimie, de Microbiologie et de Bio-informatique, Université Laval, Québec City, QC G1V 0A6, Canada; [e]Institut de Biologie Intégrative et des Systèmes, Université Laval, Québec City, QC G1V 0A6, Canada; [f]Department of Biochemistry, University of Toronto, Toronto, ON M5G 1M1, Canada; and [g]National Research Council Canada, Human Health Therapeutics, Montréal, QC H4P 2R2, Canada

Author contributions: A.M., M.E.B., P.L., E.B., and C.C. designed research; A.M., P.J., L.-J.R., M.L., C.M., and M.E.B. performed research; T.F.M. contributed new reagents/analytic tools; A.M., P.J., P.L., E.B., and C.C. analyzed data; and A.M. and C.C. wrote the paper.

1. A. H. Delcour, Outer membrane permeability and antibiotic resistance. *Biochim. Biophys. Acta* **1794**, 808–816 (2009).
2. K. M. Lehman, M. Grabowicz, Countering gram-negative antibiotic resistance: Recent progress in disrupting the outer membrane with novel therapeutics. *Antibiotics* **8**, 163 (2019).
3. H.-J. Jung, M. T. Sorbara, E. G. Pamer, TAM mediates adaptation of carbapenem-resistant Klebsiella pneumoniae to antimicrobial stress during host colonization and infection. *PLoS Pathog.* **17**, e1009309 (2021).
4. G. E. Schulz, The structure of bacterial outer membrane proteins. *Biochim. Biophys. Acta* **1565**, 308–317 (2002).
5. J. E. Horne, D. J. Brockwell, S. E. Radford, Role of the lipid bilayer in outer membrane protein folding in Gram-negative bacteria. *J. Biol. Chem.* **295**, 10340–10367 (2020).
6. J. C. Malinverni, T. J. Silhavy, Assembly of outer membrane β-barrel proteins: The bam complex. *EcoSal Plus* **4** (2011), 10.1128/ecosalplus.4.3.8.
7. J. Selkrig *et al.*, Discovery of an archetypal protein transport system in bacterial outer membranes. *Nat. Struct. Mol. Biol.* **19**, 506–510 (2012).
8. C. Stubenrauch *et al.*, Effective assembly of fimbriae in Escherichia coli depends on the translocation assembly module nanomachine. *Nat. Microbiol.* **1**, 16064 (2016).
9. C. J. Stubenrauch, T. Lithgow, The TAM: A translocation and assembly module of the β-barrel assembly machinery in bacterial outer membranes. *EcoSal Plus* **8** (2019), 10.1128/ecosalplus.ESP-0036-2018.
10. E. Heinz *et al.*, Conserved features in the structure, mechanism, and biogenesis of the inverse autotransporter protein family. *Genome Biol. Evol.* **8**, 1690–1705 (2016).
11. C. J. Stubenrauch, R. S. Bamert, J. Wang, T. Lithgow, A noncanonical chaperone interacts with drug efflux pumps during their assembly into bacterial outer membranes. *PLoS Biol.* **20**, e3001523 (2022).
12. J. Selkrig *et al.*, Conserved features in TamA enable interaction with TamB to drive the activity of the translocation and assembly module. *Sci. Rep.* **5**, 12905 (2015).
13. M. Li, B. Jia, Y. Sun, L. Sun, The translocation and assembly module (TAM) of Edwardsiella tarda is essential for stress resistance and host infection. *Front. Microbiol.* **11**, 1743 (2020).
14. R. Albrecht *et al.*, Structure of BamA, an essential factor in outer membrane protein biogenesis. *Acta Crystallogr. D Biol. Crystallogr.* **70**, 1779–1789 (2014).
15. F. Gruss *et al.*, The structural basis of autotransporter translocation by TamA. *Nat. Struct. Mol. Biol.* **20**, 1318–1320 (2013).
16. N. Noinaj, A. J. Kuszak, C. Balusek, J. C. Gumbart, S. K. Buchanan, Lateral opening and exit pore formation are required for BamA function. *Structure* **22**, 1055–1062 (2014).
17. R. S. Bamert *et al.*, Structural basis for substrate selection by the translocation and assembly module of the β-barrel assembly machinery. *Mol. Microbiol.* **106**, 142–156 (2017).
18. J. Liu, J. C. Gumbart, Membrane thinning and lateral gating are consistent features of BamA across multiple species. *PLoS Comput. Biol.* **16**, e1008355 (2020).
19. M. T. Doyle, H. D. Bernstein, BamA forms a translocation channel for polypeptide export across the bacterial outer membrane. *Mol. Cell* **81**, 2000–2012.e3 (2021).
20. C. Shen *et al.*, Structural basis of BAM-mediated outer membrane β-barrel protein assembly. *Nature* **617**, 185–193 (2023).
21. R. Wu *et al.*, Plasticity within the barrel domain of BamA mediates a hybrid-barrel mechanism by BAM. *Nat. Commun.* **12**, 7131 (2021).
22. M. T. Doyle *et al.*, Cryo-EM structures reveal multiple stages of bacterial outer membrane protein folding. *Cell* **185**, 1143–1156.e13 (2022).
23. E. Heinz, J. Selkrig, M. J. Belousoff, T. Lithgow, Evolution of the translocation and assembly module (TAM). *Genome Biol. Evol.* **7**, 1628–1643 (2015).
24. C. Calmettes, A. Judd, T. F. Moraes, Structural aspects of bacterial outer membrane protein assembly. *Adv. Exp. Med. Biol.* **883**, 255–270 (2015).
25. Y. Gu *et al.*, Structural basis of outer membrane protein insertion by the BAM complex. *Nature* **531**, 64–69 (2016).
26. P. White *et al.*, The role of membrane destabilisation and protein dynamics in BAM catalysed OMP folding. *Nat. Commun.* **12**, 4174 (2021).
27. M. N. Webby *et al.*, Lipids mediate supramolecular outer membrane protein assembly in bacteria. *Sci. Adv.* **8**, eadc9566 (2022).
28. H.-H. Shen *et al.*, Reconstitution of a nanomachine driving the assembly of proteins into bacterial outer membranes. *Nat. Commun.* **5**, 5078 (2014).
29. T. Frickey, A. Lupas, CLANS: A Java application for visualizing protein families based on pairwise similarity. *Bioinformatics* **20**, 3702–3704 (2004).
30. S. Feng, Interpretation of mechanochemical properties of lipid bilayer vesicles from the equation of state or pressure—area measurement of the monolayer at the air—water or oil—water interface. *Langmuir* **15**, 998–1010 (1999).
31. R. C. MacDonald, S. A. Simon, Lipid monolayer states and their relationships to bilayers. *Proc. Natl. Acad. Sci. U.S.A.* **84**, 4089–4093 (1987).
32. É. Boisselier, É. Demers, L. Cantin, C. Salesse, How to gather useful and valuable information from protein binding measurements using Langmuir lipid monolayers. *Adv. Colloid Interface Sci.* **243**, 60–76 (2017).
33. C. Sohlenkamp, O. Geiger, Bacterial membrane lipids: Diversity in structures and pathways. *FEMS Microbiol. Rev.* **40**, 133–159 (2016).
34. P. Calvez, É. Demers, É. Boisselier, C. Salesse, Analysis of the contribution of saturated and polyunsaturated phospholipid monolayers to the binding of proteins. *Langmuir* **27**, 1373–1379 (2011).
35. S. Morein, A. Andersson, L. Rilfors, G. Lindblom, Wild-type Escherichia coli cells regulate the membrane lipid composition in a 'window' between gel and non-lamellar structures. *J. Biol. Chem.* **271**, 6801–6809 (1996).
36. G. J. Patel, S. Behrens-Kneip, O. Holst, J. H. Kleinschmidt, The periplasmic chaperone Skp facilitates targeting, insertion, and folding of OmpA into lipid membranes with a negative membrane surface potential. *Biochemistry* **48**, 10235–10245 (2009).
37. D. Gessmann *et al.*, Outer membrane β-barrel protein folding is physically controlled by periplasmic lipid head groups and BamA. *Proc. Natl. Acad. Sci. U.S.A.* **111**, 5878–5883 (2014).
38. T. Heimburg, B. Angerstein, D. Marsh, Binding of peripheral proteins to mixed lipid membranes: Effect of lipid demixing upon binding. *Biophys. J.* **76**, 2575–2586 (1999).
39. K. Vats, K. Knutson, A. Hinderliter, E. D. Sheets, Peripheral protein organization and its influence on lipid diffusion in biomimetic membranes. *ACS Chem. Biol.* **5**, 393–403 (2010).
40. Y.-C. Lin, C. Chipot, S. Scheuring, Annexin-V stabilizes membrane defects by inducing lipid phase transition. *Nat. Commun.* **11**, 230 (2020).
41. T. Parasassi, G. De Stasio, G. Ravagnan, R. M. Rusch, E. Gratton, Quantitation of lipid phases in phospholipid vesicles by the generalized polarization of Laurdan fluorescence. *Biophys. J.* **60**, 179–189 (1991).
42. J. M. Machin, A. C. Kalli, N. A. Ranson, S. E. Radford, Protein–lipid charge interactions control the folding of outer membrane proteins into asymmetric membranes. *Nat. Chem.* **15**, 1754–1764 (2023), 10.1038/s41557-023-01319-6.
43. T. Tubiana, I. Sillitoe, C. Orengo, N. Reuter, Dissecting peripheral protein-membrane interfaces. *PLoS Comput. Biol.* **18**, e1010346 (2022).
44. G. Chwastek *et al.*, Principles of membrane adaptation revealed through environmentally induced bacterial lipidome remodeling. *Cell Rep.* **32**, 108165 (2020).
45. H. Benamara *et al.*, Characterization of membrane lipidome changes in Pseudomonas aeruginosa during biofilm growth on glass wool. *PLoS One* **9**, e108478 (2014).
46. N. Noinaj *et al.*, Structural insight into the biogenesis of β-barrel membrane proteins. *Nature* **501**, 385–390 (2013).
47. I. Josts *et al.*, The structure of a conserved domain of TamB reveals a hydrophobic β taco fold. *Structure* **25**, 1898–1906.e5 (2017).
48. M. V. Douglass, A. B. McLean, M. S. Trent, Absence of YhdP, TamB, and YdbH leads to defects in glycerophospholipid transport and cell morphology in Gram-negative bacteria. *PLoS Genet.* **18**, e1010096 (2022).
49. N. Ruiz, R. M. Davis, S. Kumar, YhdP, TamB, and YdbH are redundant but essential for growth and lipid homeostasis of the gram-negative outer membrane. *mBio* **12**, e0271421 (2021).
50. F. van den Ent, J. Löwe, RF cloning: A restriction-free method for inserting target genes into plasmids. *J. Biochem. Biophys. Methods* **67**, 67–74 (2006).
51. M. Laible, K. Boonrod, Homemade site directed mutagenesis of whole plasmids. *J. Vis. Exp.* **27**, 1135 (2009), 10.3791/1135.
52. P. D. Adams *et al.*, PHENIX: A comprehensive Python-based system for macromolecular structure solution. *Acta Crystallogr. D Biol. Crystallogr.* **66**, 213–221 (2010).
53. P. Emsley, K. Cowtan, Coot: Model-building tools for molecular graphics. *Acta Crystallogr. D Biol. Crystallogr.* **60**, 2126–2132 (2004).
54. C. J. Williams *et al.*, MolProbity: More and better reference data for improved all-atom structure validation. *Protein Sci.* **27**, 293–315 (2018).
55. M. A. Lomize, I. D. Pogozheva, H. Joo, H. I. Mosberg, A. L. Lomize, OPM database and PPM web server: Resources for positioning of proteins in membranes. *Nucleic Acids Res.* **40**, D370–D376 (2012).
56. S. Jo, T. Kim, V. G. Iyer, W. Im, CHARMM-GUI: A web-based graphical user interface for CHARMM. *J. Comput. Chem.* **29**, 1859–1865 (2008).
57. S. Jo, T. Kim, W. Im, Automated builder and database of protein/membrane complexes for molecular dynamics simulations. *PLoS One* **2**, e880 (2007).
58. J. C. Phillips *et al.*, Scalable molecular dynamics on CPU and GPU architectures with NAMD. *J. Chem. Phys.* **153**, 044130 (2020).
59. J. Huang *et al.*, CHARMM36m: An improved force field for folded and intrinsically disordered proteins. *Nat. Methods* **14**, 71–73 (2017).
60. W. L. Jorgensen, J. Chandrasekhar, J. D. Madura, R. W. Impey, M. L. Klein, Comparison of simple potential functions for simulating liquid water. *J. Chem. Phys.* **79**, 926–935 (1983).
61. S. R. Durell, B. R. Brooks, A. Ben-Naim, Solvent-induced forces between two hydrophilic groups. *J. Phys. Chem.* **98**, 2198–2202 (1994).
62. S. Miyamoto, P. A. Kollman, Settle: An analytical version of the SHAKE and RATTLE algorithm for rigid water models. *J. Comput. Chem.* **13**, 952–962 (1992).
63. J.-P. Ryckaert, G. Ciccotti, H. J. C. Berendsen, Numerical integration of the cartesian equations of motion of a system with constraints: Molecular dynamics of n-alkanes. *J. Comput. Phys.* **23**, 327–341 (1977).
64. T. Darden, D. York, L. Pedersen, Particle mesh Ewald: An $N \cdot \log(N)$ method for Ewald sums in large systems. *J. Chem. Phys.* **98**, 10089–10092 (1993).
65. U. Essmann *et al.*, A smooth particle mesh Ewald method. *J. Chem. Phys.* **103**, 8577–8593 (1995).

66. M. Seeber *et al.*, Wordom: A user-friendly program for the analysis of molecular structures, trajectories, and free energy surfaces. *J. Comput. Chem.* **32**, 1183–1194 (2011).
67. S. A. I. Seidel *et al.*, Microscale thermophoresis quantifies biomolecular interactions under previously challenging conditions. *Methods* **59**, 301–315 (2013).
68. A. Mellouk, T.F. Moraes, C. Calmettes, $P2_1$ Crystal structure of TamA from Pseudomonas aeruginosa at 2.6 angstrom. Protein Data Bank. https://www.rcsb.org/structure/8US1. Deposited 27 October 2023.
69. A. Mellouk, T.F. Moraes, C. Calmettes, $P22_12_1$ Crystal structure of TamA from Pseudomonas aeruginosa at 3.95 angstrom. Protein Data Bank. https://www.rcsb.org/structure/8US2. Deposited 27 October 2023.
70. A. Mellouk, T.F. Moraes, C. Calmettes, C2 Crystal structure of TamA from Pseudomonas aeruginosa at 3.1 angstrom. Protein Data Bank. https://www.rcsb.org/structure/8US3. Deposited 27 October 2023.
71. A. Mellouk, T.F. Moraes, C. Calmettes, $C222_1$ Crystal structure of TamA (β-barrel only) from Pseudomonas aeruginosa at 3.15 angstrom. Protein Data Bank. https://www.rcsb.org/structure/8US4. Deposited 27 October 2023.